Journal of Optics

PAPER

Plasmonic crystal with independently tunable double resonances

To cite this article: Xinan Xu *et al* 2020 *J. Opt.* **22** 095007

View the article online for updates and enhancements.

You may also like

- An equivalent method of multi-beam laser interference lithography for 2D plasmonic crystals fabrication
Chen Liu, Cheng Zhang, Hui Wang et al.
- Fabrication of uniform diffraction gratings using laser interference lithography for simultaneous measurement of refractive index
Sungjae Lee, Yongwon Ma, Junhan Park et al.
- Lattice plasmons in dielectric nanoparticle arrays arranged on metal film
Lianxue Zhang, Chaoyang Ge, Kun Zhang et al.

IOP ebooks™

Bringing together innovative digital publishing with leading authors from the global scientific community.

Start exploring the collection–download the first chapter of every title for free.

This content was downloaded from IP address 221.6.40.189 on 10/03/2022 at 06:38

IOP Publishing Journal of Optics
J. Opt. **22** (2020) 095007 (6pp) https://doi.org/10.1088/2040-8986/ababe8

Plasmonic crystal with independently tunable double resonances

Xinan Xu[1,2], **Jinwu Dong**[1,2], **Shuai Chen**[1] **and Xianyu Ao**[1]

Centre for Optical and Electromagnetic Research, South China Academy of Advanced Optoelectronics, South China Normal University, Guangzhou 510006, People's Republic of China

E-mail: optixy@m.scnu.edu.cn

Received 10 June 2020, revised 15 July 2020
Accepted for publication 2 August 2020
Published 25 August 2020

Abstract

This paper reports the design and fabrication of large-area periodic arrays of metal nanostructures that can support dual-wavelength resonance with spatially overlapping hot spots. Gold films with protruding posts arranged in a rectangular lattice are stripped from silicon templates containing shallow hole arrays, defined by laser interference lithography. The plasmonic resonances at the band edges for the two orthogonal linear polarizations can be tuned independently by changing the corresponding lattice spacing. WSe_2 monolayers and IR-140 dye molecules demonstrate directional and linearly polarized photoluminescence when coupled with such plasmonic crystals. The anisotropic lattice can enable enhancements at both the excitation and emission wavelengths. The emission is preferentially coupled to the first diffraction orders of the plasmonic crystals, resulting in a directional beam.

Keywords: surface plasmon, double resonances, interference lithography, photoluminescence, polarization anisotropy

(Some figures may appear in colour only in the online journal)

1. Introduction

Plasmonic resonances, the collective electronic oscillations at the surface of metals, have an unprecedented ability to localize electromagnetic fields and boost light–matter interactions in nanoscale volumes [1]. The spectral and spatial features of plasmonic resonances strongly depend on the shape, size, and arrangement of the noble metal nanostructures. For some specific applications, structures supporting resonances at two or more wavelengths with spatially overlapping hot spots are highly desired. For example, in surface-enhanced Raman spectroscopy (SERS), higher enhancement factors can be achieved with resonances at both the excitation and Raman scattering frequencies, compared to similar structures with single resonance [2–5], as the SERS enhancement factor is proportional to the product of the electric field intensity enhancements at the excitation and Raman scattering frequencies. Similar arguments also hold for other scenarios with matched resonances at both the excitation and emission wavelengths, such as lasing [6], upconversion [7] and nonlinear harmonic generation [8–11], where the former can enhance the absorption at the pump wavelength and the latter can enhance the radiative decay of the generated signal. On the other hand, plasmonic structures with multiple resonances can allow multiple molecular vibrational modes to be detected simultaneously [12], or multi-wavelength lasing [13, 14].

For most of the plasmonic structures mentioned above, the underlying mechanism required to generate two or more resonances and the corresponding fabrication processes are rather complicated. As an example, in [11], independent tunability was realized by tuning the thickness of the dielectric spacer and the size of the metal nanoparticles, which involved different fabrication processes. By contrast, it is relatively easy to tune resonances by adjusting the lattice spacing of periodic arrays. Resonant wavelengths can be set precisely by the lattice spacing, as the lattice spacing is a very reproducable quantity when using beam-based writing techniques and photolithography. In this regard, plasmonic crystals—optically thick metal films with periodic patterns, can offer a wide range of tunability [15–17]. Moreover, patterned metal films with smooth surfaces can

[2] These authors contributed equally to this work.

 © 2020 IOP Publishing Ltd Printed in the UK

be prepared by template stripping to reduce the scattering loss [18].

Here we show plasmonic resonances with spatially overlapping hot spots based on plasmonic crystals with rectangular lattices, for which the resonant wavelengths can be tuned independently by changing the corresponding lattice spacing. In comparison with 2D square lattices and 1D gratings, a rectangular lattice has additional degrees of freedom. We fabricated plasmonic crystals using laser interference lithography (LIL) and the template stripping method. We further demonstrated directional and linearly polarized photoluminescence from WSe_2 monolayers and IR-140 dye molecules coupled to such plasmonic crystals. The anisotropic lattice enabled enhancements at both the excitation and emission wavelengths.

2. Results and discussion

Figure 1(a) depicts the plasmonic crystal considered here, consisting of a metal film with protruding metal posts in a rectangular lattice. We noticed that a metal nanoparticle on a metal film can scatter light in a different manner, compared to a metal nanoparticle in free space. For a metal nanoparticle on a metal film, the scattered field radiated parallel to the applied electric field (figure 1(b)), whereas for a metal particle in free space the scattered field radiated perpendicularly to the applied electric field (figure 1(c)). Therefore, one can expect that the tunability that results from the diffractive coupling in a film-type plasmonic crystal is different from the tunability of plasmonic lattices composed of metal nanoparticles. The tunability of film-type plasmonic crystals with varying y-spacings (a_y) is illustrated in simulated normal-incidence reflection spectra (figure 1(d)), where the x-spacing ($a_x = 740$ nm) and post size ($d_x = 330$ nm, $d_y = 450$ nm, and $h = 50$ nm) are fixed. The simulation was performed by the finite difference time domain (FDTD) method and the optical constants of gold were taken from Johnson and Christy [19]. In the FDTD, we set perfectly matched layer boundary conditions for the z direction, and periodic boundary conditions for the x and y directions of the simulation region, with a uniform mesh size of 2 nm, and we used broadband plane wave excitation. When the incident electric field was parallel to the x-axis, the position of the longer-wavelength resonance remained constant, whereas the shorter-wavelength resonance shifted to longer wavelengths as a_y increased. In contrast, when the incident electric field was parallel to the y-axis, the longer-wavelength resonance shifted linearly with a_y, whereas the shorter-wavelength resonance shifted much less. As will be shown later, these longer-wavelength resonances are related to $(\pm 1, 0)$ diffraction orders, and therefore, the most important parameter determining the resonant wavelength is the spacing in the direction parallel to the incident electric field.

Figure 2(a) depicts the fabrication procedure used to prepare plasmonic crystals, by combining LIL and the template stripping method. Figure 2(b) shows our LIL setup based on Lloyd's mirror interferometer [20]. The beam from a He-Cd laser was spatially filtered through a pinhole and expanded to illuminate both the mirror and the sample. Part of the light was

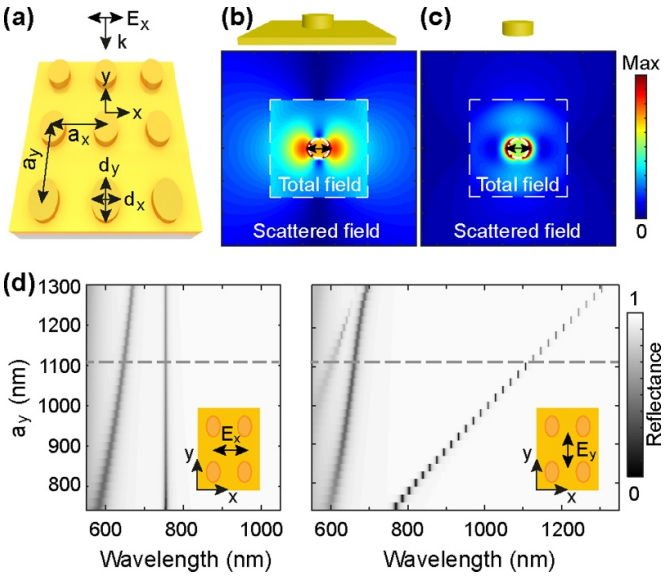

Figure 1. (a) A schematic of the plasmonic crystal with gold posts in a rectangular lattice on a gold film. (b), (c) Scattering by a gold particle (diameter $d = 300$ nm, height $h = 50$ nm) on a gold film and in free space, respectively, at a 750 nm wavelength at normal incidence. The electric field amplitude is recorded at the bottom surface of the particle. The polarization of the applied electric field is indicated by the double-arrow. (d) Simulated reflection spectra at normal incidence with varying values of a_y (while $a_x = 740$ nm, $d_x = 330$ nm, $d_y = 450$ nm, and $h = 50$ nm are fixed) for the film-type plasmonic crystal. The inset indicates the corresponding polarization of the incident electric field.

reflected by the mirror surface and interfered with the portion of the beam that was directly illuminating the sample. A single exposure can produce a periodic line pattern. The lattice spacing of the line pattern can be tuned by the motorized rotation stage at the bottom as $a_{x,y} = \lambda_0/\sin(\theta)$, where λ_0 is the wavelength of the He-Cd laser (i.e. 325 nm) and θ the incident angle. A second exposure was made after rotating the sample ($\varphi = 90°$) with another motorized rotation stage to form the rectangular lattice. A thin layer of aluminum (~10 nm) was then deposited on the photoresist post array produced by LIL and lifted off to generate aluminum nanoholes. We obtained silicon templates by reactive ion etching (~50 nm deep) of the silicon substrates through the aluminum mask, resulting in a 2D rectangular array of silicon holes. Finally, we deposited ~150 nm thick gold onto the silicon templates by e-beam evaporation, and stripped the gold film using a UV curable adhesive (NOA 61, Norland). Our fabrication procedure can produce samples with areas over 1 cm^2 at a low cost (figure 2(c)). Figure 2(d) shows the scanning electron microscope (SEM) image of a stripped gold film which was designed to match the emission of direct-gap semiconducting WSe_2 monolayers (A exciton, ~1.63 eV) [21–23].

Figures 3(a) and (b) show the normal-incidence reflection spectra of the fabricated plasmonic crystal ($a_x = 740$ nm, $a_y = 1110$ nm, $d_x = 330$ nm, $d_y = 450$ nm, and $h = 50$ nm) under illumination by x- and y-polarized light, respectively, measured with an optical microscope (with a 1.25X/0.03NA objective, Zeiss) coupled to a spectrometer (iHR550, Horiba).

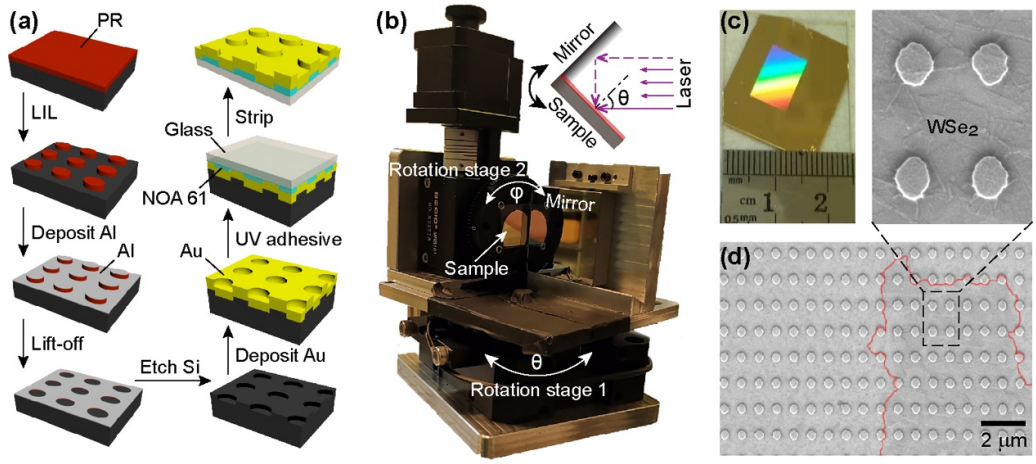

Figure 2. (a) A schematic of the fabrication procedure, performed by combining laser interference lithography (LIL) and the template stripping method. (b) A photograph of the Lloyd's mirror interferometer on motorized rotation stages. (c) A photograph of a typical sample. (d) A SEM image of the plasmonic crystal with a lattice spacing $a_x = 740$ nm and $a_y = 1110$ nm. The marked area with darker contrast is covered with WSe_2 monolayers.

For each polarization, two strong resonances can be identified as two deep dips, and the main features of the measurement were reproduced well by the simulation. The two reflection dips were at $\lambda_I = 650$ nm and $\lambda_{II} = 756$ nm for the x-polarization, and $\lambda_{III} = 662$ nm and $\lambda_{IV} = 1117$ nm for the y-polarization. We transferred chemical vapor deposition (CVD)-grown WSe_2 monolayers from the growth substrate onto the plasmonic crystal using water-soluble polymer films as a sacrificial mediator [24]. For WSe_2 monolayers, the center wavelength of emission is around 760 nm, and thus only polarization parallel to the x-axis can be enhanced by the plasmonic resonance at $\lambda_{II} = 756$ nm, while shorter-wavelength resonances can be tuned to the excitation wavelength to enhance the pump absorption. The anisotropic lattice can enable independently tunable resonances with spatially overlapping hot spots for enhancing both excitation and emission. Excitation and emission can share almost-identical mode profiles to maximize the spatial overlap of their enhancements (figures 3(c) and (d)). The WSe_2 monolayers formed a conformal contact with the gold structure (figure 2(d)), and the resonances were slightly shifted to longer wavelengths due to the increase of the surrounding refractive index from the monolayers.

Angle-resolved photoluminescence and reflection spectra were measured to map out the angular distribution of fluorescence and the dispersion diagram (figures 4(a) and (b)). In our measurement setup, the incident beams (from the 532 nm laser used to excite photoluminescence, and supercontinuum white light for reflection) were collinear and fixed [24]. For the reflection measurement, both the sample and the collection probe (including a 0.25NA lens and a multimode fiber) were rotated within the plane of incidence to keep the collection probe at the specular position of the incident beam; for photoluminescence measurement, only the collection probe was rotated. The collected signal was guided to a compact spectrometer (QE65 Pro, Ocean Optics). For simplicity, we only show here the results with the polarization aligned to the x-axis; the fluorescence intensity of the other polarization was much weaker.

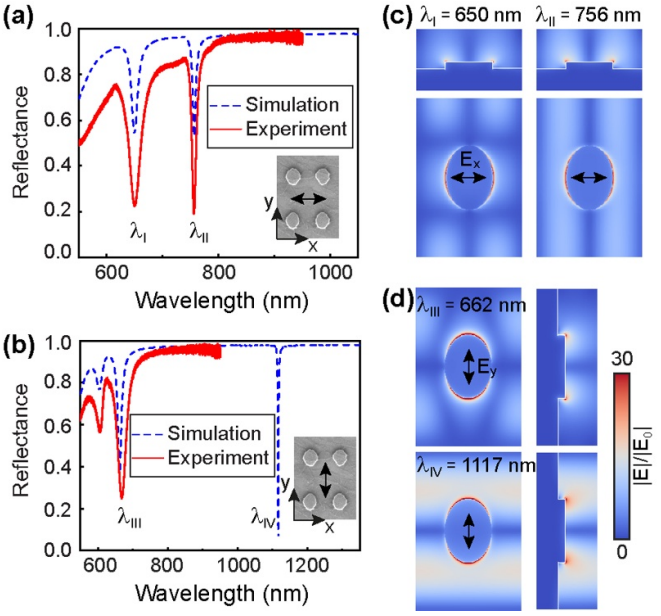

Figure 3. (a), (b) Reflection spectra at normal incidence for the plasmonic crystal ($a_x = 740$ nm, $a_y = 1110$ nm, $d_x = 330$ nm, $d_y = 450$ nm, and $h = 50$ nm) with polarization of the incident light parallel to the x- and y-axis, respectively. (c), (d) Electric field profiles at the reflection drop-offs. The arrows indicate the polarization of the incident light.

The dispersion diagram of the plasmonic crystal determines the far field emission pattern. The surface plasmon modes in the plasmonic crystal obey the dispersion relation [18],

$$\mathrm{Re}\left[k_0\sqrt{\frac{\varepsilon_m\varepsilon_d}{\varepsilon_m+\varepsilon_d}}\right] = \left|k_0(\sin\theta_x\hat{\mathbf{u}}_x + \sin\theta_y\hat{\mathbf{u}}_y) + i\frac{2\pi}{a_x}\hat{\mathbf{u}}_x + j\frac{2\pi}{a_y}\hat{\mathbf{u}}_y\right|,$$

where k_0 is the free-space wave number, ε_m and ε_d are the permittivity of the metal and dielectric, respectively, $\hat{\mathbf{u}}_x$ and $\hat{\mathbf{u}}_y$ are unitary vectors along the x- and y-axes, and (i, j) are

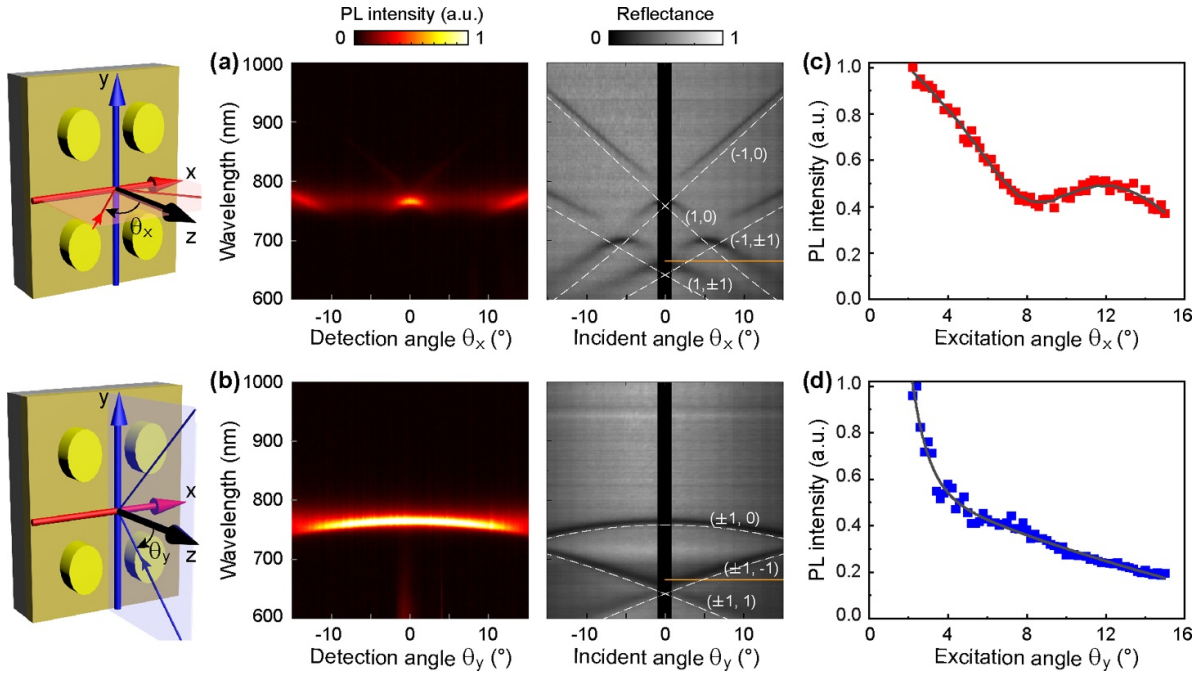

Figure 4. (a), (b) An angle-resolved mapping of the photoluminescence (PL) and reflection spectra. For reflection, the incident white light is polarized along the *x*-axis. For PL, the excitation beam ($\lambda_{ex} = 532$ nm) is incident at an angle of 20° and polarized perpendicularly to the scan plane, and the analyzer for emission is polarized along the *x*-axis. (c), (d) The PL peak intensity as a function of the excitation angle (using a 660 nm laser). The solid lines are a guide to the eye. The angular scanning is in the *xz*-plane for (a), (c) and in the *yz*-plane for (b), (d), respectively, as illustrated in the drawings on the left.

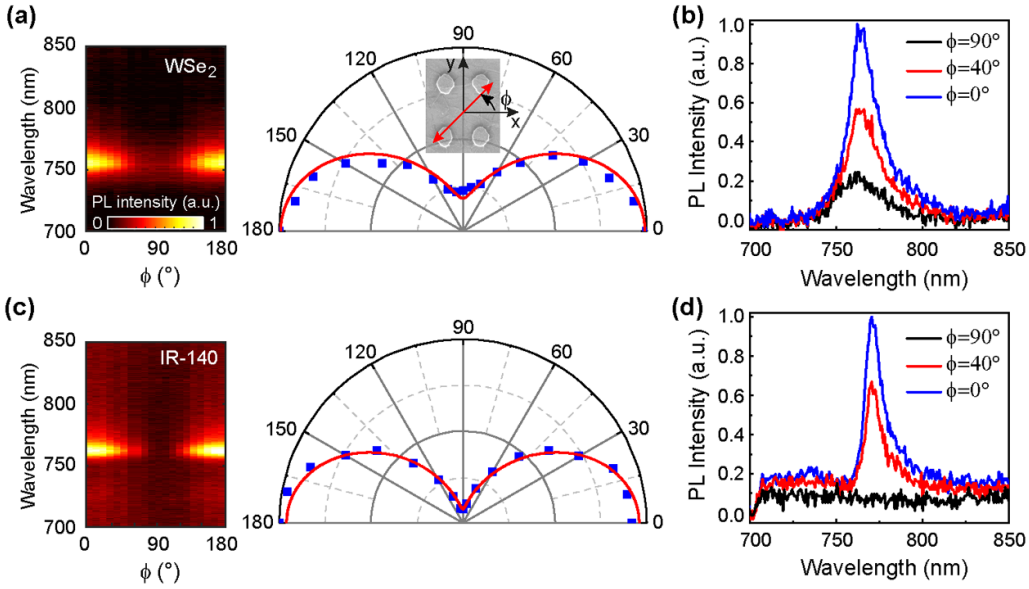

Figure 5. The emission spectra and polar plots of the peak PL intensity versus the angle of the polarization analyzer Φ. (a), (b) WSe_2 monolayers. (c), (d) SU-8 film doped with IR-140 dye molecules (~15 nm thick). The excitation beam ($\lambda_{ex} = 660$ nm) is incident at an angle of 20°, and at this angle no resonances exist at the excitation wavelength.

diffraction orders. We overlaid this dispersion relation as the dashed lines on the reflection in figures 4(a) and (b). The emission in the *xz*-plane (figure 4(a), transverse-magnetic (TM) polarization) was mainly coupled to the (±1, 0) diffraction orders, and the brightest spot was at 0° where the two (±1, 0) branches formed an intersection. The side lobe beyond 10° in the *xz*-plane was coupled to the (−1, ±1) orders and can be tuned by adjusting a_y. The emission in the *yz*-plane (figure 4(b), transverse-electric (TE) polarization) was coupled to the (±1, 0) diffraction orders which were degenerate and quadratic, and the emission intensity faded out as the detection angle approached 15° because the resonances moved out of the emission band of WSe_2. As explained in figures 1(b) and (c), the diffractive coupling in our plasmonic crystal is different

compared to rectangular arrays of metal nanoparticles [25], where the role of TE and TM polarizations are interchanged.

The PL intensity is proportional to the absorbed energy at the excitation wavelength. To study the enhancement at the excitation wavelength, we chose a 660 nm laser (Cobolt) as the pump light and scanned the excitation angle from 2° to 15° (marked by an orange line in the reflection maps in figures 4(a) and (b)). The peak intensity of the emission spectra as a function of the excitation angle is shown in figures 4(c) and (d). When scanned in the *xz*-plane (figure 4(c), TM polarization), resonances were seen at around 0° and 11° at the excitation wavelength, and correspondingly, there were local maxima around the excitation angles of 0° and 11° in the peak intensity plot (the data for $\theta < 2°$ were not available). When scanned in the *yz*-plane (figure 4(d), TE polarization), there was only one resonance at around 0°, and the peak intensity decreased as the excitation angle increased from 2° to 15°. This dependence on the excitation angle is attributed to the enhancement of the pump absorption by resonances at the excitation wavelength.

Polarization-resolved measurement of the emission (collected along the surface normal) revealed that the emission was linearly polarized along the *x*-axis (figure 5(a)). The excitation beam ($\lambda_{ex} = 660$ nm) was incident at an angle of 20°, and at this excitation angle, no resonances existed for the excitation wavelength. We found that the polarization of the emission did not rely on the polarization of the excitation beam, but the emission intensity did vary as the excitation polarization changed (due to polarization-dependent absorption). The polarization anisotropy of emission was $\rho = 0.64$ [defined as $\rho = (I_x – I_y)/(I_x + I_y)$, with I_x and I_y the emission intensities of linear polarization along the *x*- and *y*-axes, respectively]. We attribute this modest ρ value to the relatively low polarization-selective emission enhancement in this particular sample covered with WSe_2. For polarization parallel to the *y*-axis at normal incidence, the plasmonic crystal behaved like a flat gold film at the emission wavelength, because no resonances existed (figure 3(b)), and the emission polarized along the *y*-axis could not be suppressed. The enhancement of the emission polarized along the *x*-axis relative to that polarized along the *y*-axis was about 4.5 times (figure 5(b)), and this relative enhancement factor was close to the value (~5.2) reported for WSe_2 monolayers on a 760 nm-spacing square lattice of 9 nm wide trenches in gold [26]. A higher polarization-selective enhancement can improve the polarization anisotropy of emission. Figures 5(c) and (d) show another plasmonic crystal coated with a 15 nm thick SU-8 film doped with IR-140 dye molecules [27], where $\rho = 0.85$ was achieved, corresponding to a polarization-selective enhancement of about 12 times. Unlike the CVD-grown WSe_2 monolayers, the SU-8 film made by spin coating covered the plasmonic crystal uniformly. The polarization-selective enhancement can be further improved by tuning the height of the protruding metal posts [18] and also optimizing the surface roughness of the protruding posts to reduce the loss.

3. Conclusions

In summary, we have introduced a plasmonic crystal that can support independently tunable double resonances with spatially overlapping hot spots. The fabrication was based on LIL and the template stripping method. We further demonstrated linearly polarized and directional emission from WSe_2 monolayers and IR-140 dye molecules coupled with such a plasmonic crystal. The rectangular lattice can provide a polarization-selective enhancement at the emission wavelengths, and can therefore enhance only one polarization of the emission, even though the emitters are randomly oriented. This scheme works especially well for emitters with a low intrinsic quantum efficiency. The directionality of emission comes from the coupling with diffraction orders. The ability to tailor the directionality and polarization of the emission using a large-area lithography technique provides prospects for application in a new generation of nanosized light sources and compact light-emitting devices [28].

Acknowledgments

This work was partially supported by Natural Science Foundation of Guangdong Province (2018A0303130056, 2020A1515010491)

ORCID iD

Xianyu Ao https://orcid.org/0000-0003-1987-849X

References

[1] Fernández-Domínguez A I, García-Vidal F J and Martín-Moreno L 2017 Unrelenting plasmons *Nat. Photon.* **11** 8–10
[2] Chu Y, Banaee M G and Crozier K B 2010 Double-resonance plasmon substrates for surface-enhanced Raman scattering with enhancement at excitation and stokes frequencies *ACS Nano* **4** 2804–10
[3] Banaee M G and Crozier K B 2011 Mixed dimer double-resonance substrates for surface-enhanced raman spectroscopy *ACS Nano* **5** 307–14
[4] Lin J, Zhang Y, Qian J and He S 2014 A nano-plasmonic chip for simultaneous sensing with dual-resonance surface-enhanced Raman scattering and localized surface plasmon resonance *Laser Photon. Rev.* **8** 610–6
[5] Lin J, Zhang Y, Lee E-H and He S 2015 A triple-resonance Raman chip for simultaneous enhancement of stokes and anti-stokes lines utilizing both localized and non-localized plasmonic resonance *J. Opt.* **17** 105001
[6] Zhu Z H, Liu H, Wang S M, Ye W M, Yuan X D and Zhu S N 2010 Double-resonance nanolaser based on coupled slit-hole resonator structures *Opt. Lett.* **35** 754–6
[7] Liu X and Lei D Y 2015 Simultaneous excitation and emission enhancements in upconversion luminescence using plasmonic double-resonant gold nanorods *Sci. Rep.* **5** 15235
[8] Aouani H, Navarro-Cia M, Rahmani M, Sidiropoulos T P H, Hong M, Oulton R F and Maier S A 2012 Multiresonant broadband optical antennas as efficient tunable nanosources of second harmonic light *Nano Lett.* **12** 4997–5002
[9] Thyagarajan K, Rivier S, Lovera A and Martin O J F 2012 Enhanced second-harmonic generation from double resonant plasmonic antennae *Opt. Express* **20** 12860–5
[10] Celebrano M *et al* 2015 Mode matching in multiresonant plasmonic nanoantennas for enhanced second harmonic generation *Nat. Nanotechnol.* **10** 412–7

[11] Zeng Y, Qian H, Rozin M J, Liu Z and Tao A R 2018 Enhanced second harmonic generation in double-resonance colloidal metasurfaces *Adv. Funct. Mater.* **28** 1803019
[12] Chen K, Adato R and Altug H 2012 Dual-band perfect absorber for multispectral plasmon-enhanced infrared spectroscopy *ACS Nano* **6** 7998–8006
[13] Wang D, Yang A, Wang W, Hua Y, Schaller R D, Schatz G C and Odom T W 2017 Band-edge engineering for controlled multi-modal nanolasing in plasmonic superlattices *Nat. Nanotechnol.* **12** 889–94
[14] Winkler J M, Ruckriegel M J, Rojo H, Keitel R C, De Leo E, Rabouw F T and Norris D J 2020 Dual-wavelength lasing in quantum-dot plasmonic lattice lasers *ACS Nano* **14** 5223–32
[15] Gao H, Zhou W and Odom T W 2010 Plasmonic crystals: a platform to catalog resonances from ultraviolet to near-infrared wavelengths in a plasmonic library *Adv. Funct. Mater.* **20** 529–39
[16] Li Z, Butun S and Aydin K 2014 Ultranarrow band absorbers based on surface lattice resonances in nanostructured metal surfaces *ACS Nano* **8** 8242–8
[17] Zhou W, Gao H and Odom T W 2010 Toward broadband plasmonics: tuning dispersion in rhombic plasmonic crystals *ACS Nano* **4** 1241–7
[18] Yang A, Li Z, Knudson M P, Hryn A J, Wang W, Aydin K and Odom T W 2015 Unidirectional lasing from template-stripped two-dimensional plasmonic crystals *ACS Nano* **9** 11582–8
[19] Johnson P B and Christy R W 1972 Optical constants of the noble metals *Phys. Rev.* B **6** 4370–9
[20] de Boor J, Kim D S and Schmidt V 2010 Sub-50 nm patterning by immersion interference lithography using a Littrow prism as a Lloyd's interferometer *Opt. Lett.* **35** 3450–2
[21] Mak K F and Shan J 2016 Photonics and optoelectronics of 2D semiconductor transition metal dichalcogenides *Nat. Photon.* **10** 216–26
[22] Dai Z, Hu G, Ou Q, Zhang L, Xia F, Garcia-Vidal F J, Qiu C W and Bao Q 2020 Artificial metaphotonics born naturally in two dimensions *Chem. Rev.* **120** 6197–246
[23] Hu G *et al* 2019 Coherent steering of nonlinear chiral valley photons with a synthetic Au–WS2 metasurface *Nat. Photon.* **13** 467–72
[24] Ao X, Xu X, Dong J and He S 2018 Unidirectional enhanced emission from 2D monolayer suspended by dielectric pillar array *ACS Appl. Mater. Interfaces* **10** 34817–21
[25] Le-Van Q, Zoethout E, Geluk E J, Ramezani M, Berghuis M and Gómez Rivas J 2019 Enhanced quality factors of surface lattice resonances in plasmonic arrays of nanoparticles *Adv. Opt. Mater.* **7** 1801451
[26] Wang Z *et al* 2016 Giant photoluminescence enhancement in tungsten-diselenide–gold plasmonic hybrid structures *Nat. Commun.* **7** 11283
[27] Ao X, Wang D and Odom T W 2019 Enhanced fields in mirror-backed low-index dielectric structures *ACS Photon.* **6** 2612–7
[28] Lozano G, Louwers D J, Rodríguez S R K, Murai S, Jansen O T A, Verschuuren M A and Rivas J G 2013 Plasmonics for solid-state lighting: enhanced excitation and directional emission of highly efficient light sources *Light Sci. Appl.* **2** e66